Supplementary Information

Breaking the Rate-Limiting Barrier in Solid-Solid Sulfur Redox Reactions via Spin-State Engineering

In the format provided by the authors and unedited

Contents

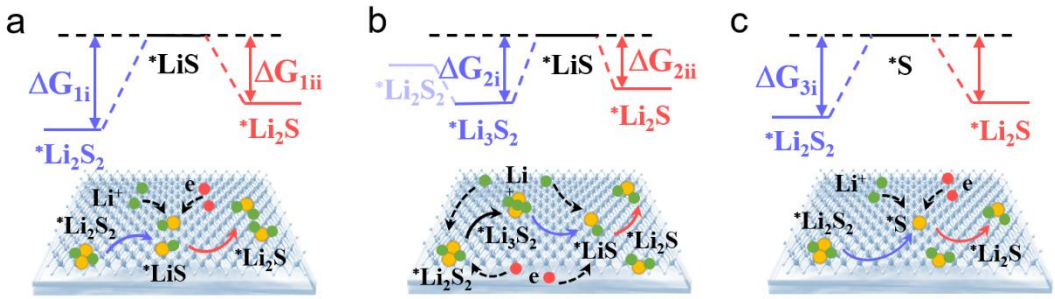

Supplementary Fig. 1 | Schematic of the three possible reaction paths in converting Li_2S_2 to Li_2S. a, $*Li_2S_2$ - *LiS - $*Li_2S$. b, $*Li_2S_2$ - $*Li_3S_2$ - *LiS - $*Li_2S$. c, $*Li_2S_2$ - *S - $*Li_2S$. The yellow and green spheres represent the S and Li atoms, respectively.

Pathway 1:

$$*Li_2S_2 + * \rightarrow 2*LiS \quad (1i)$$

$$2*LiS + 2Li^+ + 2e^- \rightarrow 2*Li_2S \quad (1ii)$$

Pathway 2:

$$(*Li_2S_2 + Li^+ + e^- \rightarrow *Li_3S_2)$$

$$*Li_3S_2 + * \rightarrow *LiS + *Li_2S \quad (2i)$$

$$*LiS + Li^+ + e^- \rightarrow *Li_2S \quad (2ii)$$

Pathway 3:

$$*Li_2S_2 + * \rightarrow *S + *Li_2S \quad (3i)$$

$$*S + 2Li^+ + 2e^- \rightarrow *Li_2S \quad (3ii)$$

Supplementary Fig. 2 | The detailed reaction equation for the formation of three possible intermediates (*LiS, $*Li_3S_2$, and *S) during the Li_2S_2 to Li_2S reaction's three possible reaction paths.

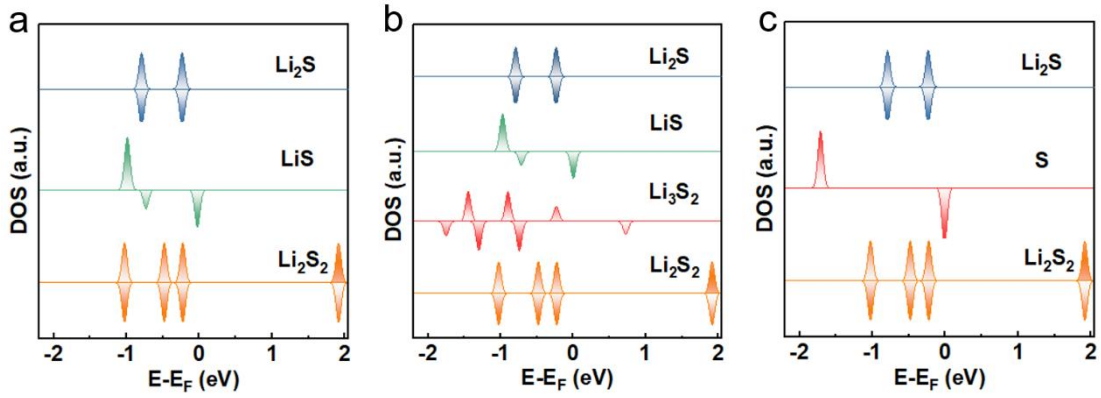

Supplementary Fig. 3 | The DOS of each transition state of a, *Li_2S_2 - *LiS - *Li_2S, b, *Li_2S_2 - *Li_3S_2 - *LiS - *Li_2S, c, *Li_2S_2 - *S - *Li_2S.

Pathway 1

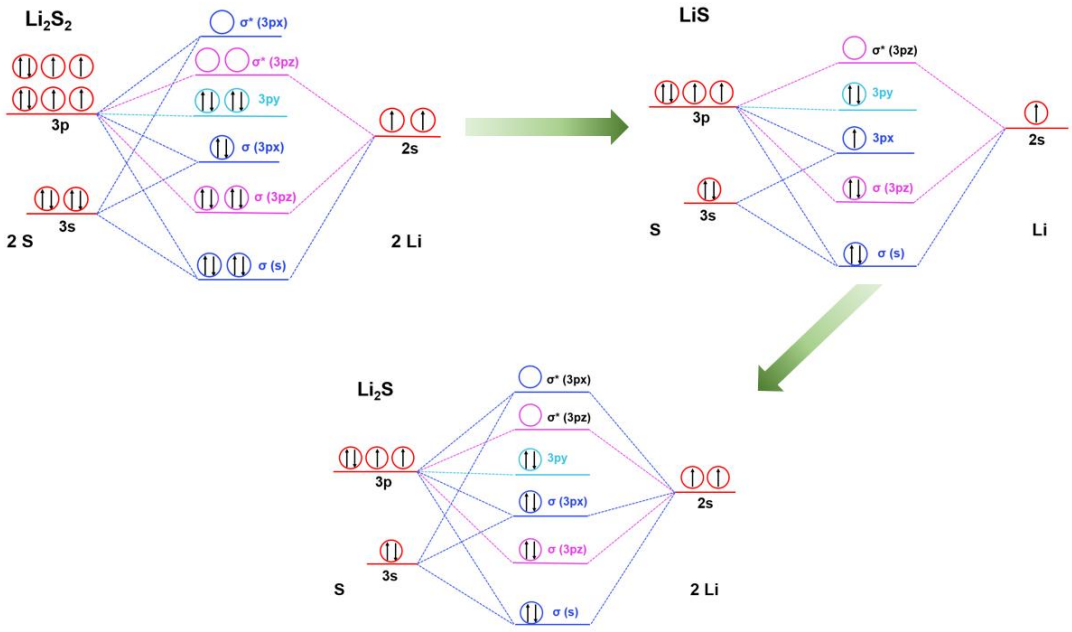

Supplementary Fig. 4 | Schematic of the degeneracy of molecular orbitals in path 1, (Li_2S_2 - LiS - Li_2S).

Pathway 2

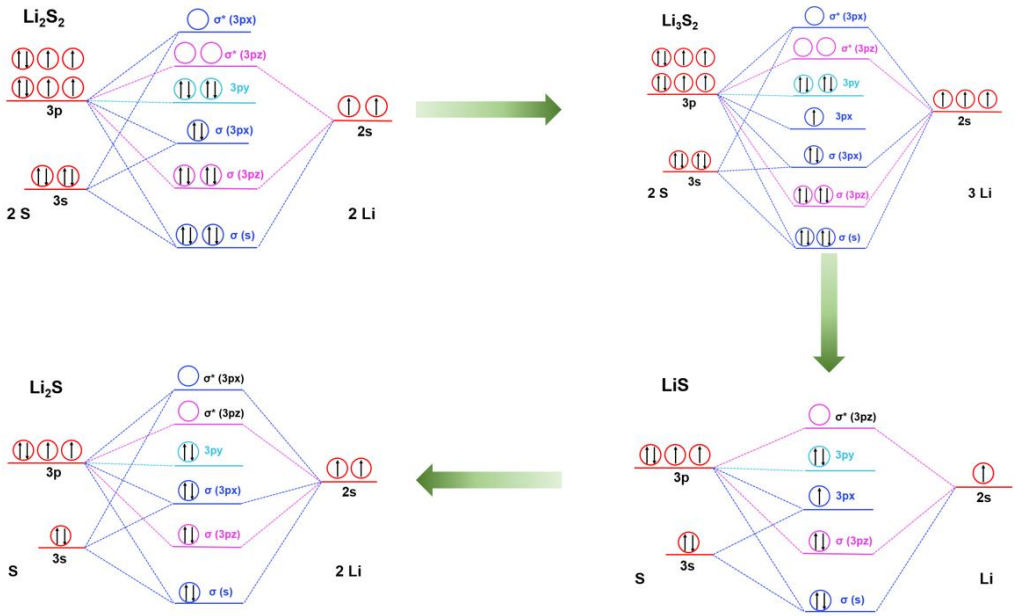

Supplementary Fig. 5 | Schematic of the degeneracy of molecular orbitals in path 2 (Li_2S_2 - Li_3S_2 - LiS - Li_2S).

Pathway 3

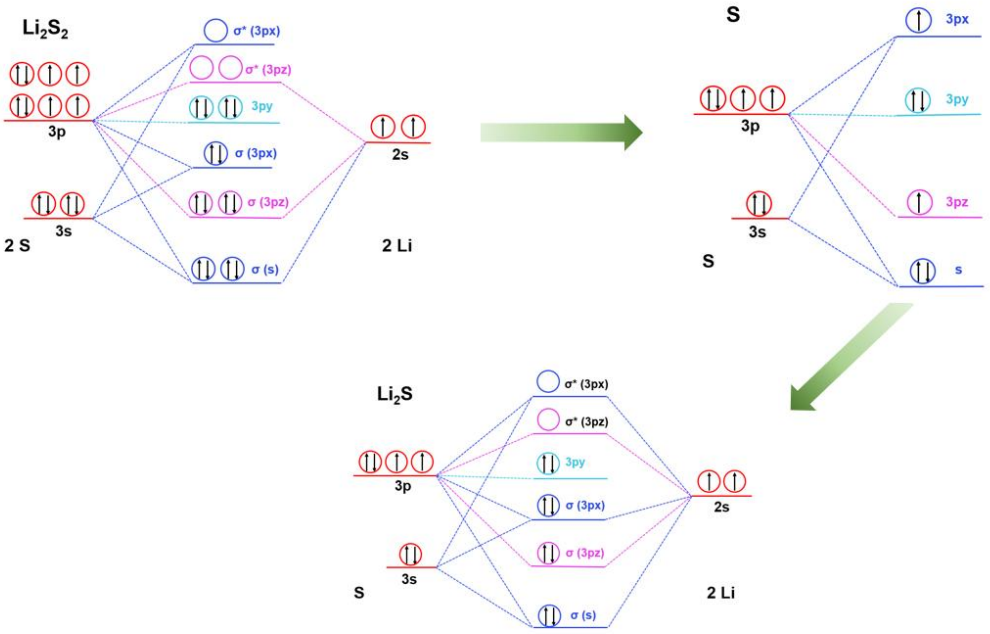

Supplementary Fig. 6 | Schematic of the degeneracy of molecular orbitals in path 3 (Li_2S_2 - S - Li_2S).

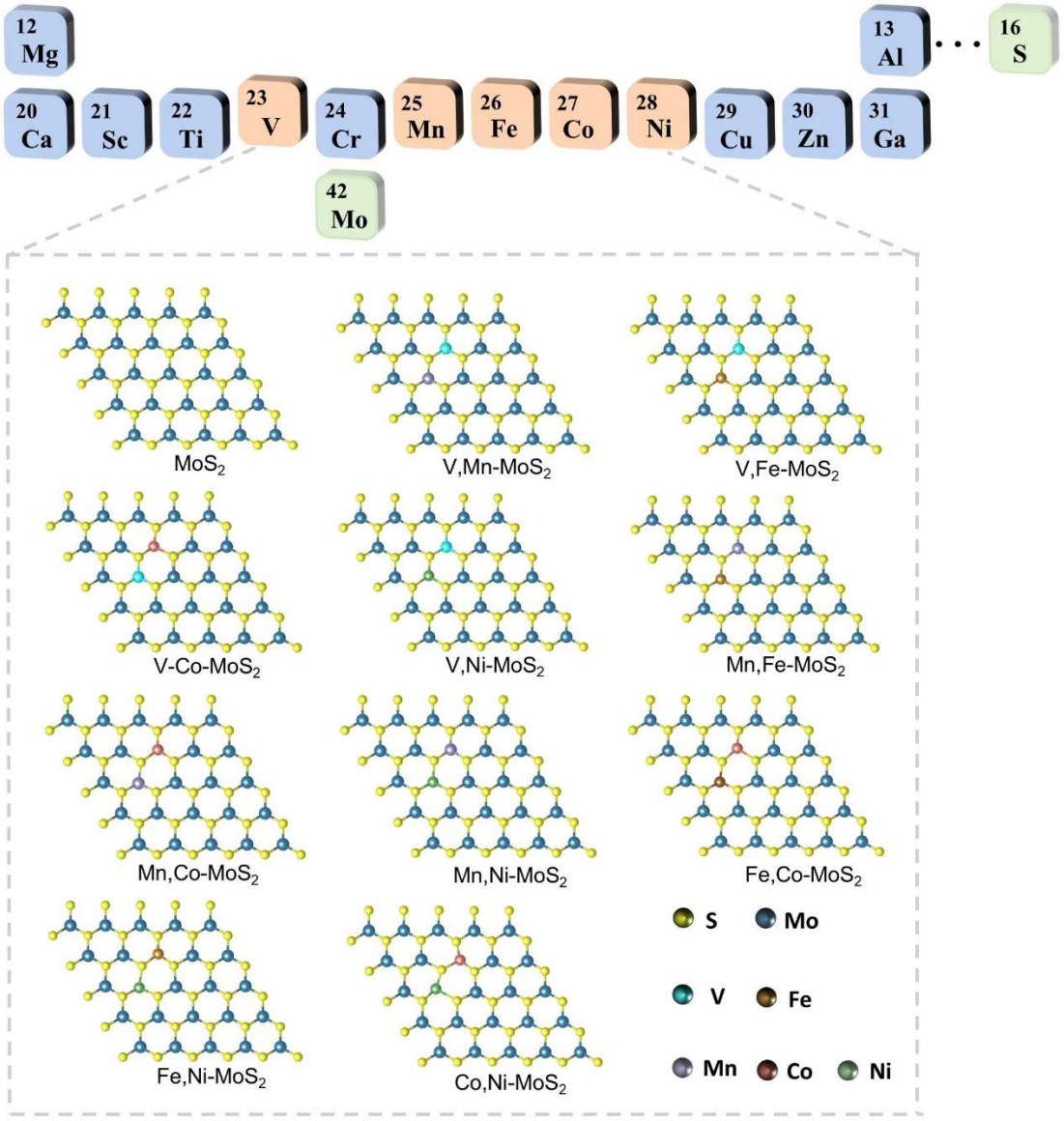

Supplementary Fig. 7 | The optimized structures of pristine MoS_2 and ten MoS_2 materials doped with two different atoms.

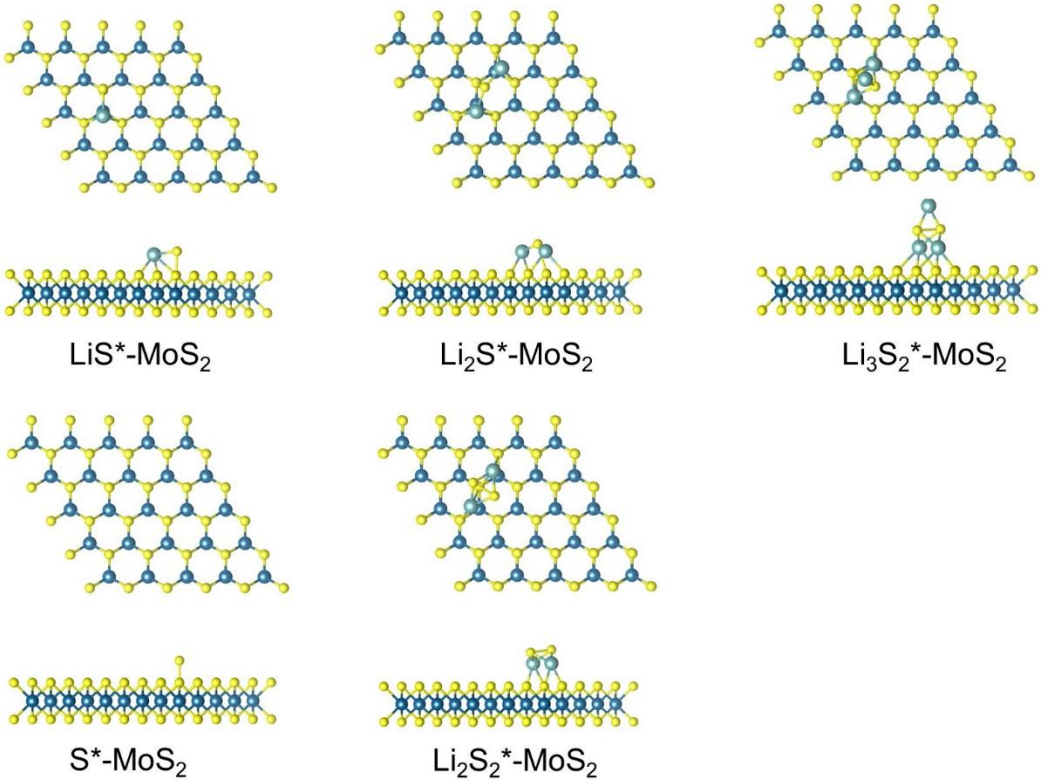

Supplementary Fig. 8 | The optimized structures of the initial state *Li_2S_2, three intermediates (*LiS, *Li_3S_2, and *S), and the final state *Li_2S on the MoS_2 surface. Yellow, blue, and green spheres denote S, Mo, and Li atoms, respectively.

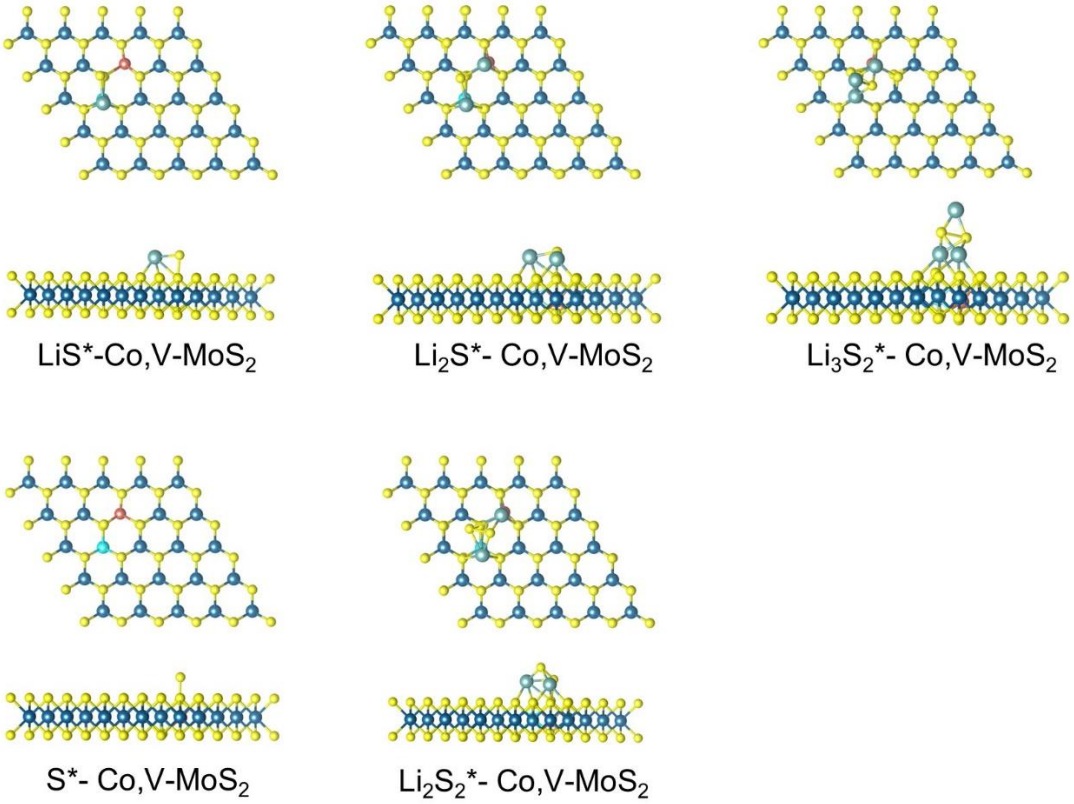

Supplementary Fig. 9 | The optimized structures of initial state *Li_2S_2, three intermediates (*LiS, *Li_3S_2, and *S), and final state *Li_2S on the Co,V-MoS_2 surface. Yellow, blue, slight blue, cyan, and pink spheres denote S, Mo, Li, V, and Co atoms, respectively.

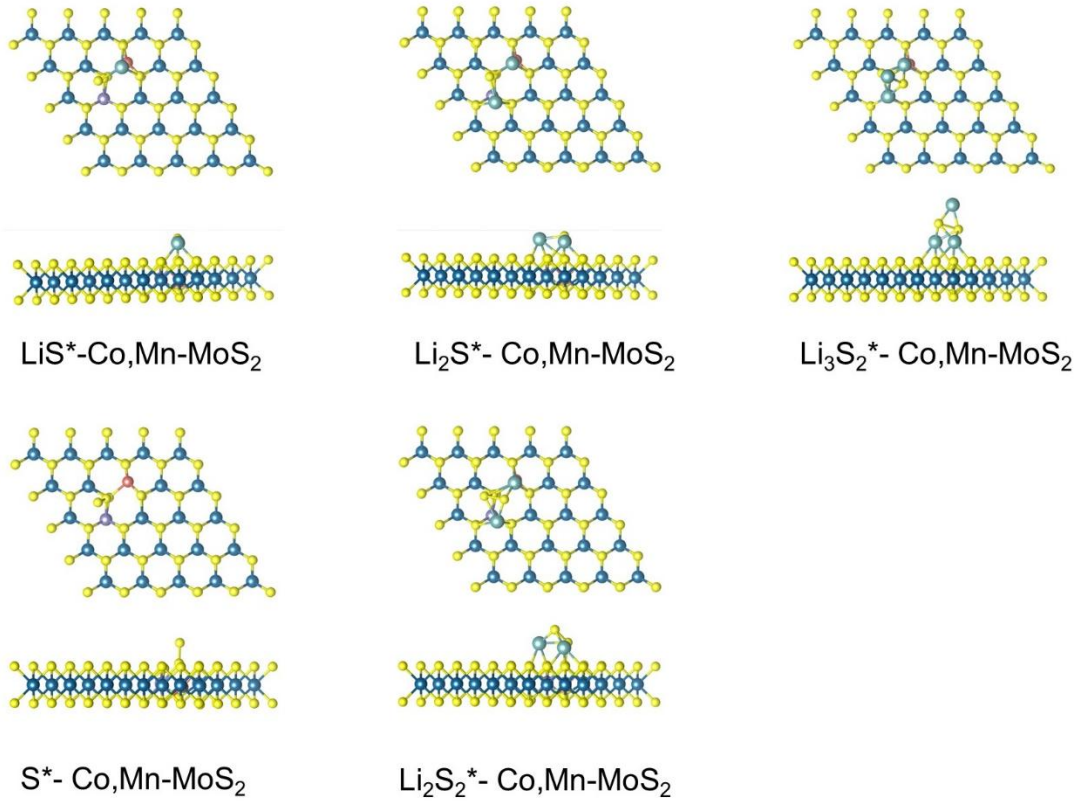

Supplementary Fig. 10 | The optimized structures of initial state *Li_2S_2, three intermediates (*LiS, *Li_3S_2, and *S), and final state *Li_2S on the Co,Mn-MoS_2 surface. Yellow, blue, slight blue, purple, and pink spheres denote S, Mo, Li, Mn, and Co atoms, respectively.

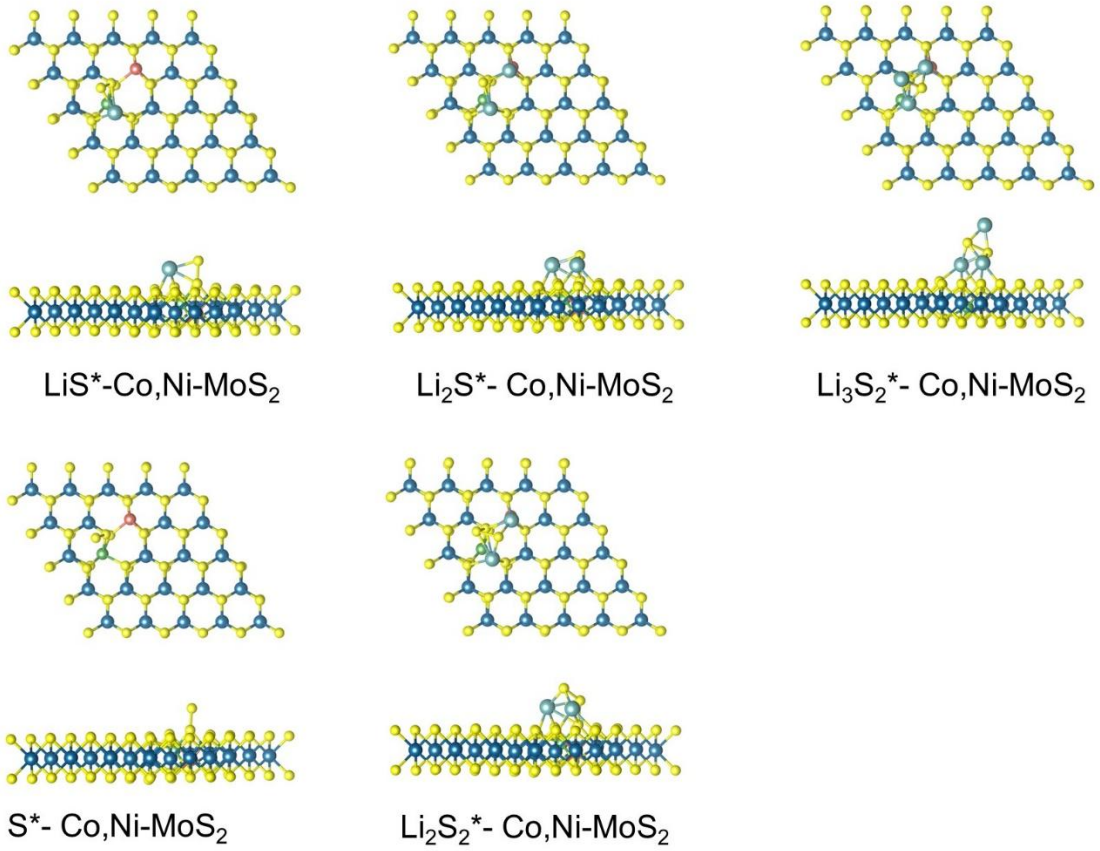

Supplementary Fig. 11 | The optimized structures of initial state *Li_2S_2, three intermediates (*LiS, *Li_3S_2, and *S), and final state *Li_2S on the Co,Ni-MoS_2 surface. Yellow, blue, slight blue, green, and pink spheres denote S, Mo, Li, Ni, and Co atoms, respectively.

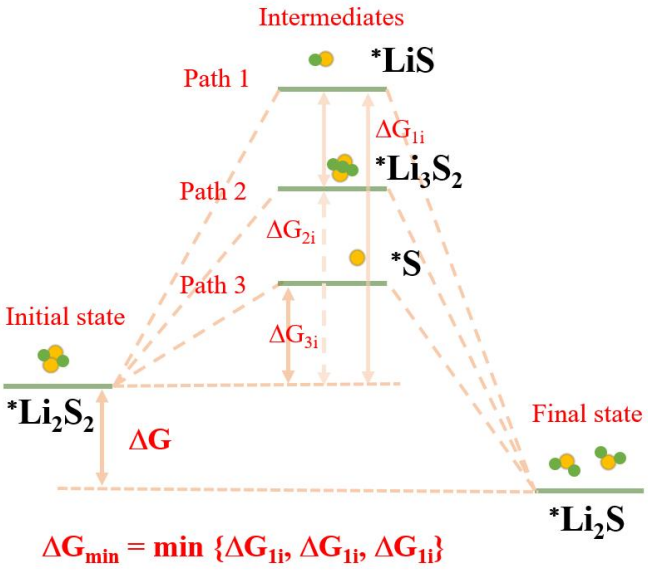

Supplementary Fig. 12 | Schematic of the Gibbs free energy charge (ΔG) between Li_2S_2, Li_2S, and the different intermediates.

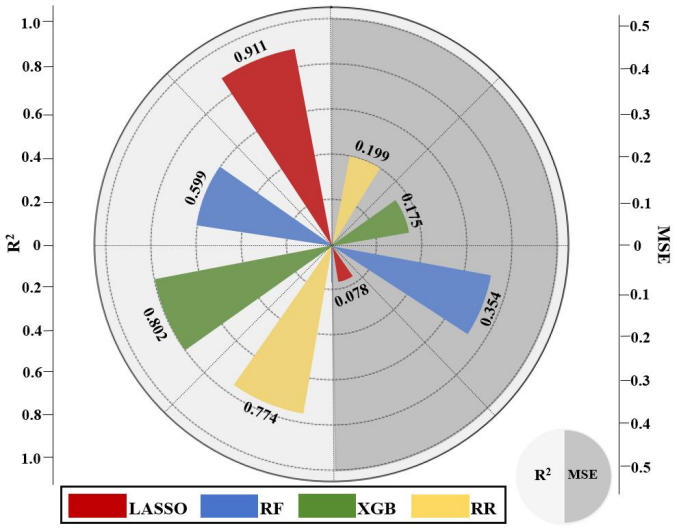

Supplementary Fig. 13 | The R^2 and MSE from optimal ML models, including the LASSO (Least Absolute Shrinkage and Selection Operator) model, the RF (Random Forest) model, the XGB (Extreme Gradient Boosting) model, and the RR (Ridge Regression) model.

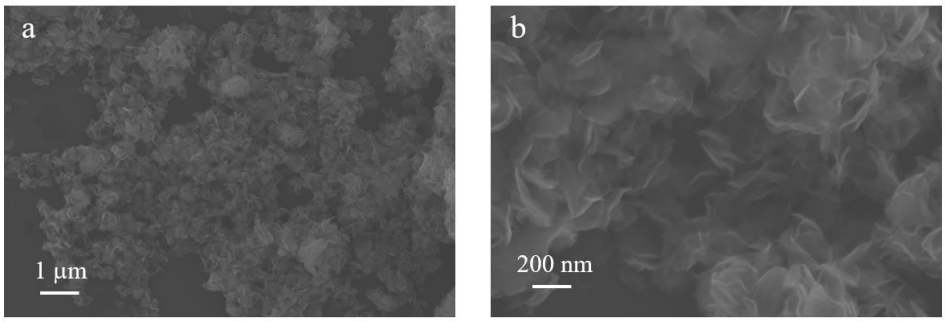

Supplementary Fig. 14 | The morphology of MoS_2. **a**, SEM image, **b**, TEM image.

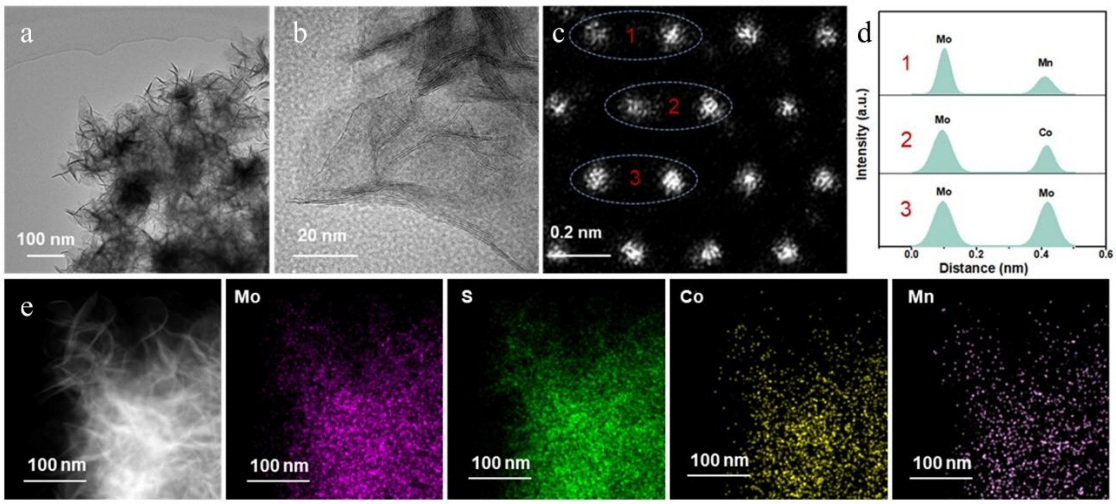

Supplementary Fig. 15 | The morphology of Co,Mn-MoS_2, **a**, TEM image, **b**, HRTEM image. **c**, HAADF-STEM image, **d**, the corresponding linear intensity profiles, and **e**, the elemental EDS maps.

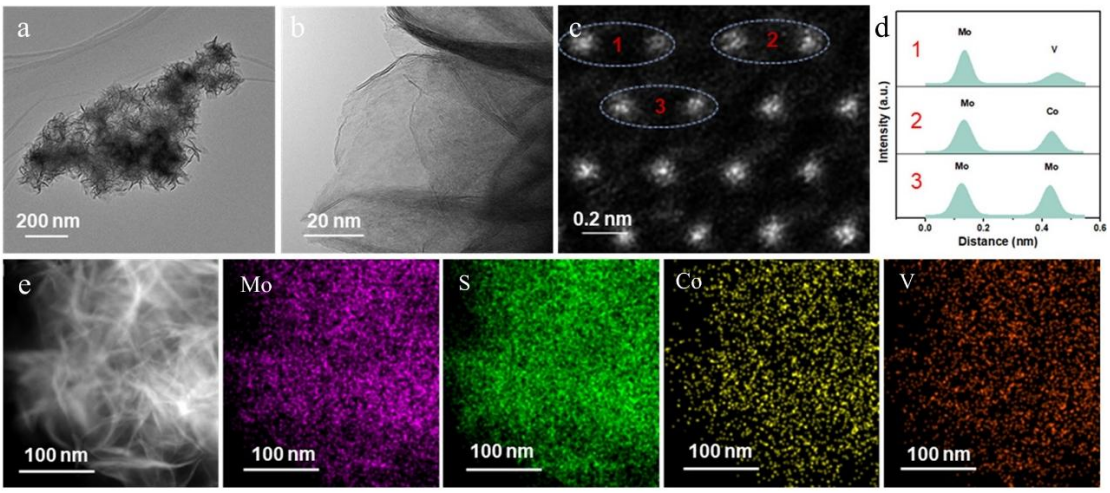

Supplementary Fig. 16 | The morphology of Co,V-MoS_2, **a**, TEM image, **b**, HRTEM image. **c**, HAADF-STEM image, **d**, the corresponding linear intensity profiles, and **e**, the elemental EDS maps.

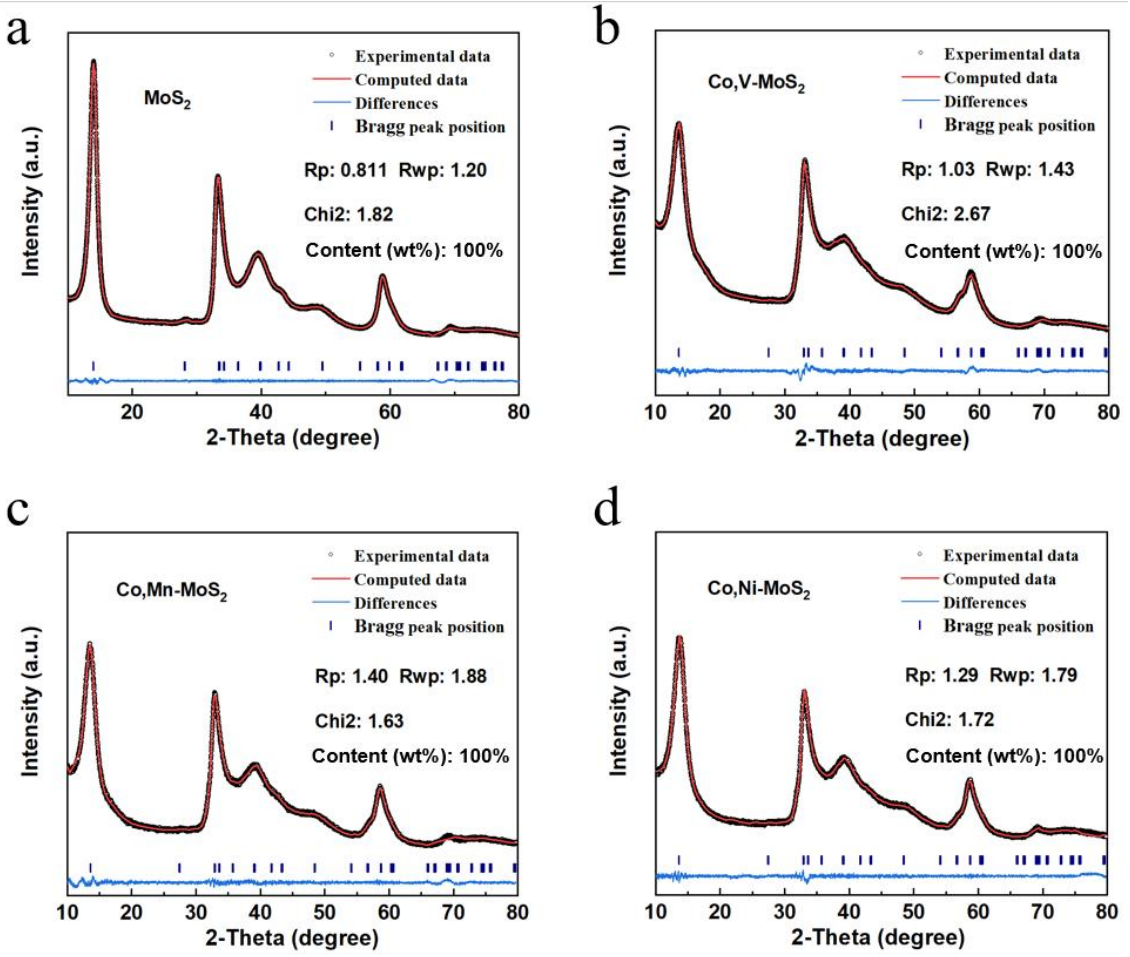

Supplementary Fig. 17 | Rietveld refinement XRD patterns for **a**, MoS_2, **b**, Co,V-MoS_2, **c**, Co,Mn-MoS_2, and **d**, Co,Ni-MoS_2.

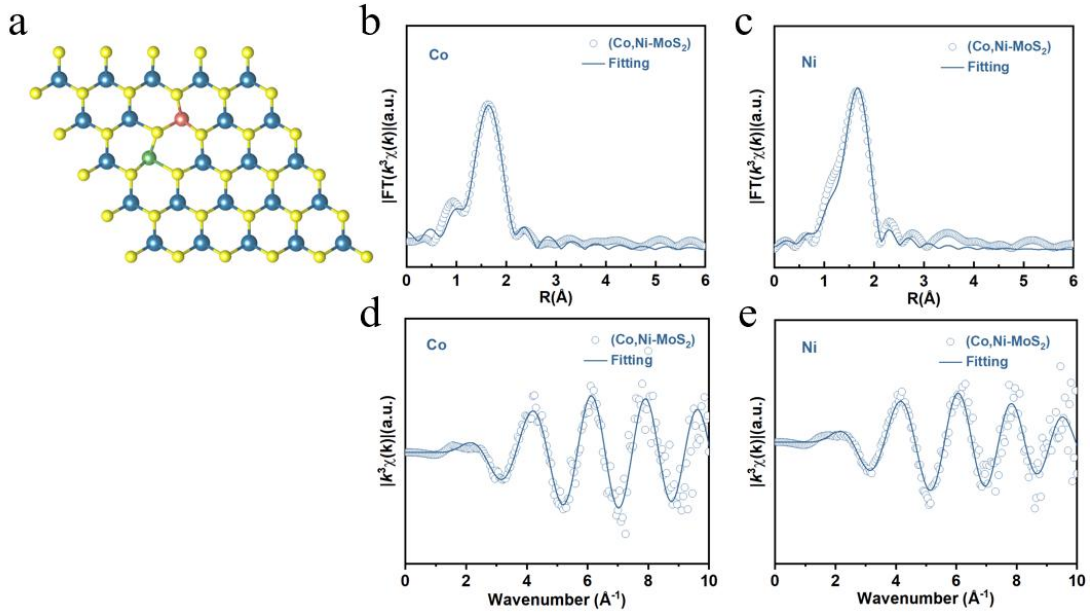

Supplementary Fig. 18 | a, The atom structure of Co,Ni-MoS_2 obtained by DFT. **b**, Co K-edge and **c**, Ni K-edge EXAFS fitting spectra of the Co,Ni-MoS_2. **d**, The corresponding Co K-edge and **e**, Ni K-edge EXAFS oscillations were extracted from the K-edge spectra of this material in k space.

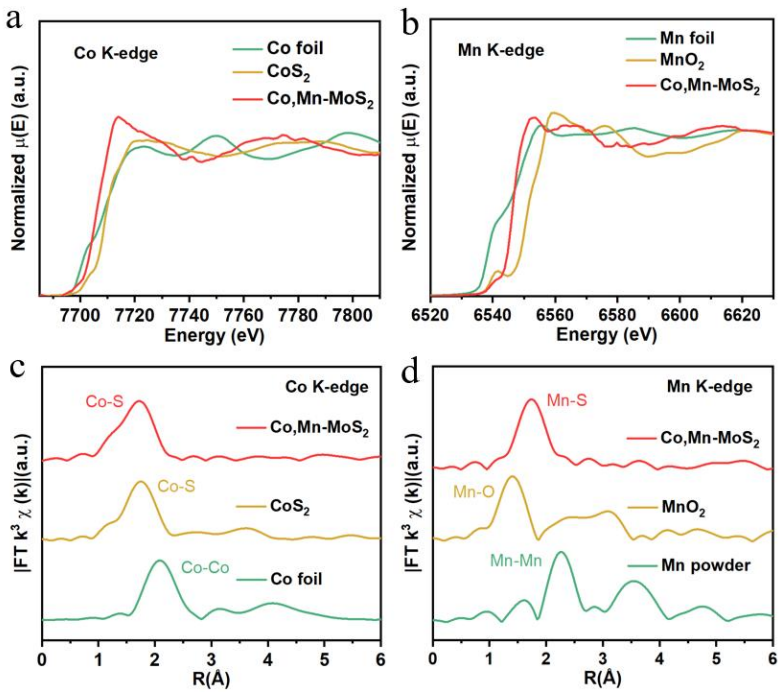

Supplementary Fig. 19 | a, The Co K-edge and **b**, Mn K-edge XANES spectra of Co,Mn-MoS_2. **c** and **d**, the corresponding fourier-transform k^3-weighted EXAFS spectra of the samples.

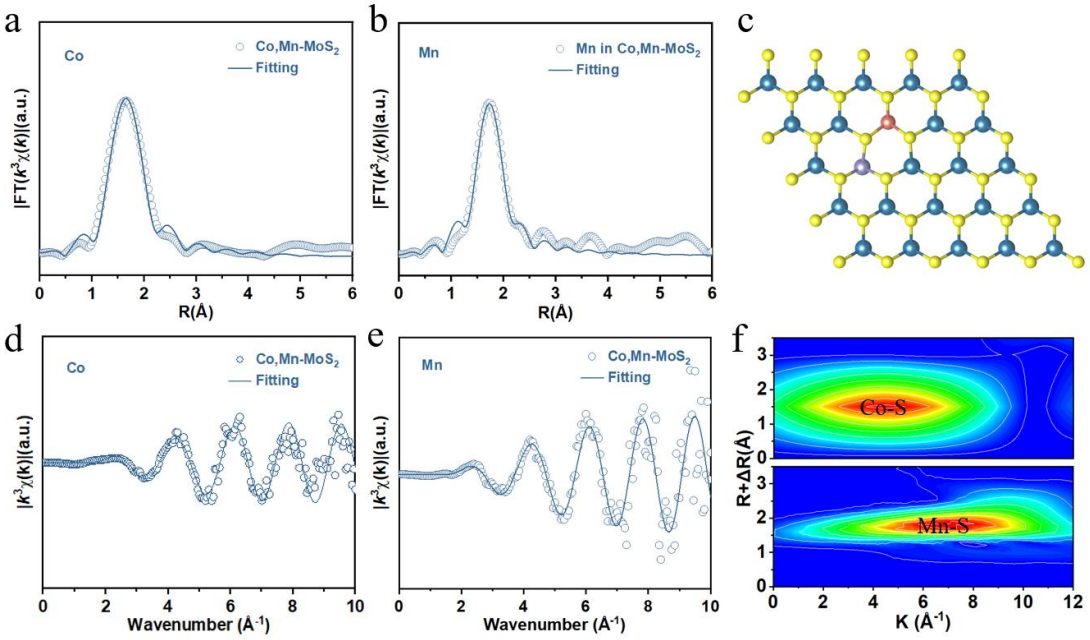

Supplementary Fig. 20 | a, The Co K-edge and **b**, Mn K-edge EXAFS fit spectra of Co,Mn-MoS_2. **c**, The atomic structure of Co,Mn-MoS_2 obtained by DFT. **d**, The corresponding Co K-edge and **e**, Mn K-edge EXAFS oscillations extracted from the K-edge spectra of the composites in k space. **f**, The corresponding wavelet-transform contour plots of the EXAFS signal of the samples.

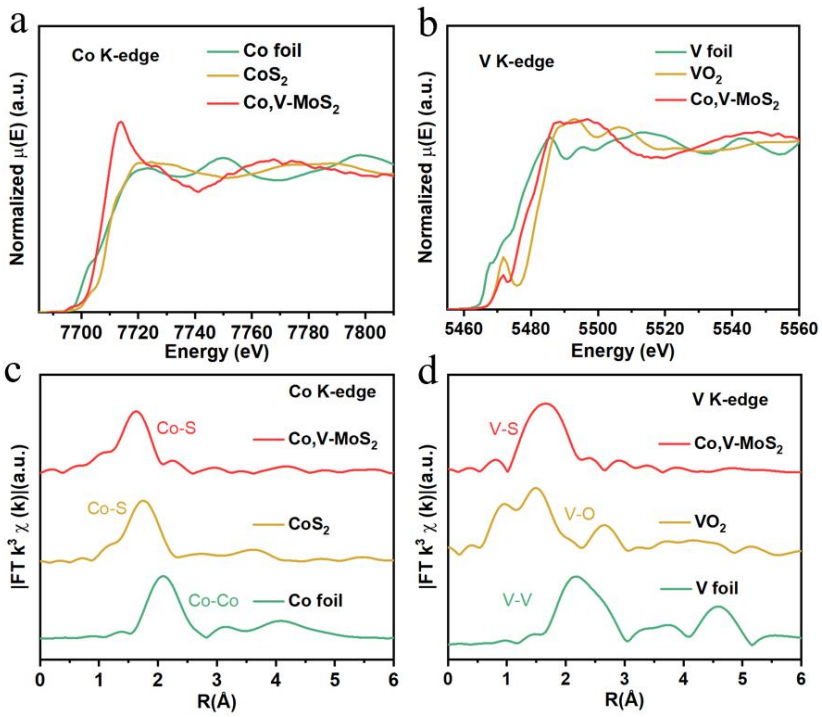

Supplementary Fig. 21 | a, The Co K-edge and **b**, V K-edge XANES spectra of Co,V-MoS_2. **c** and **d,** the corresponding fourier-transform k^3-weighted EXAFS spectra of the samples.

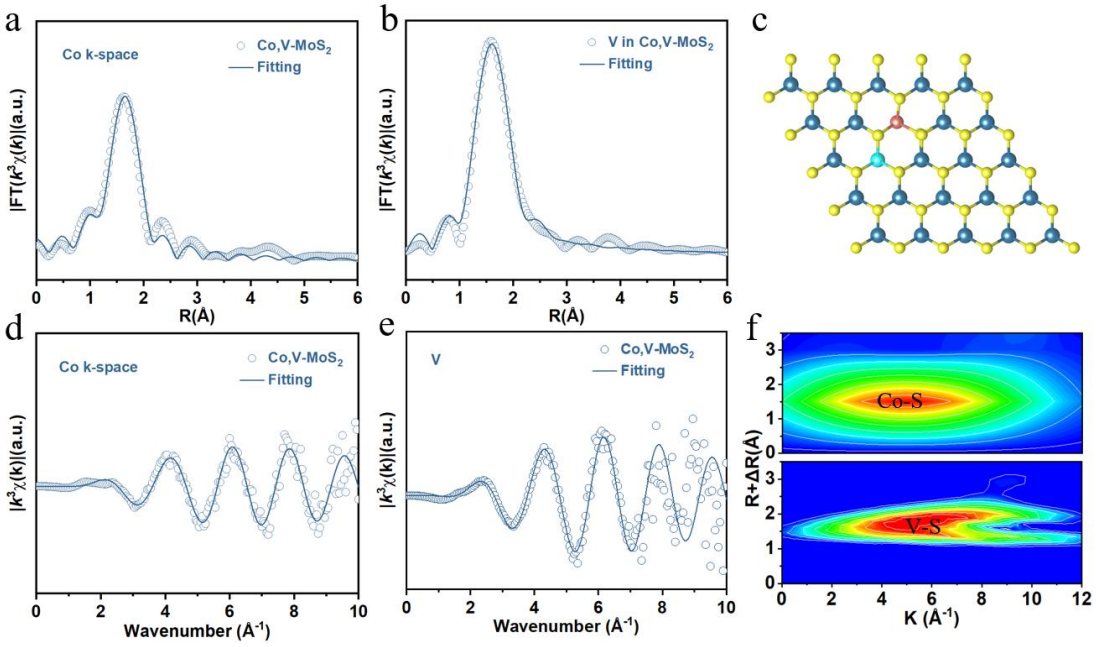

Supplementary Fig. 22 | a, The Co K-edge and **b**, V K-edge EXAFS fiting spectra of Co,V-MoS_2. **c**, The atomic structure of Co,V-MoS_2 obtained by DFT. **d**, The corresponding Co K-edge and **e**, Mn K-edge EXAFS oscillations extracted from K-edge spectra of the composites in k space. **f**, The corresponding wavelet-transform contour plots of the EXAFS signal of the samples.

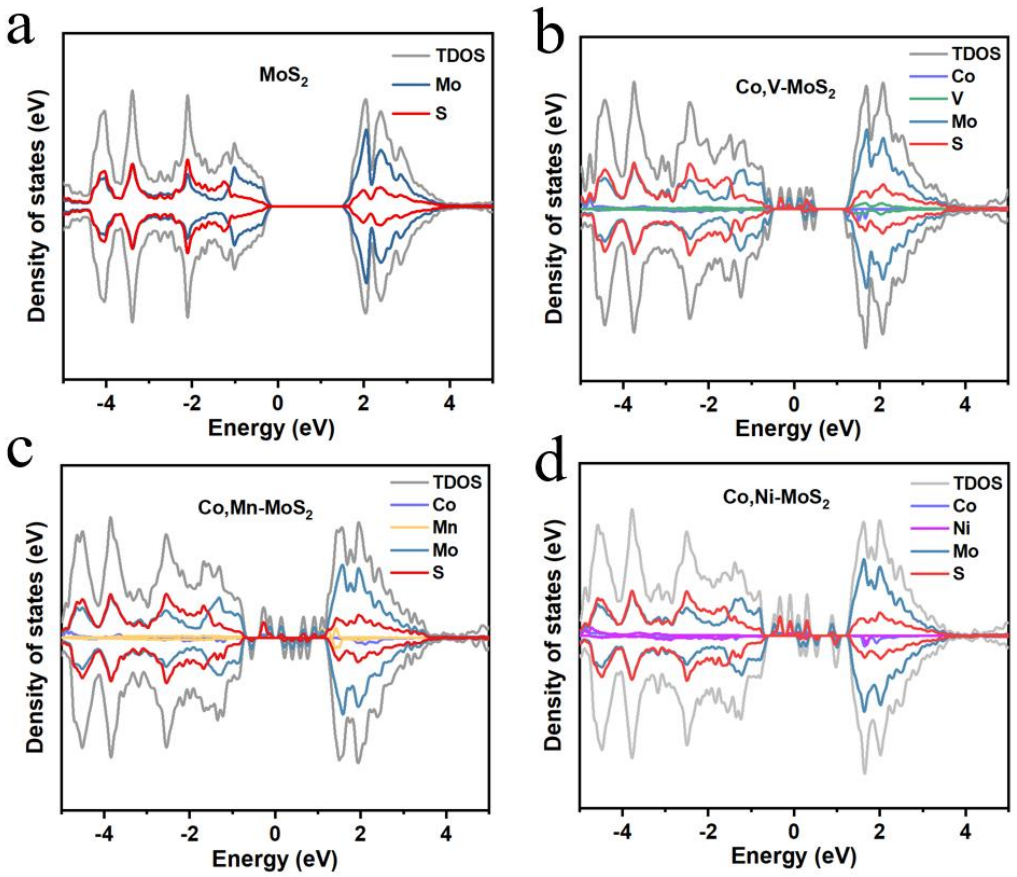

Supplementary Fig. 23 | The calculated DOS near the Fermi level for **a**, MoS_2, **b**, Co,V-MoS_2, **c**, Co,Mn-MoS_2, **d**, Co,Ni-MoS_2.

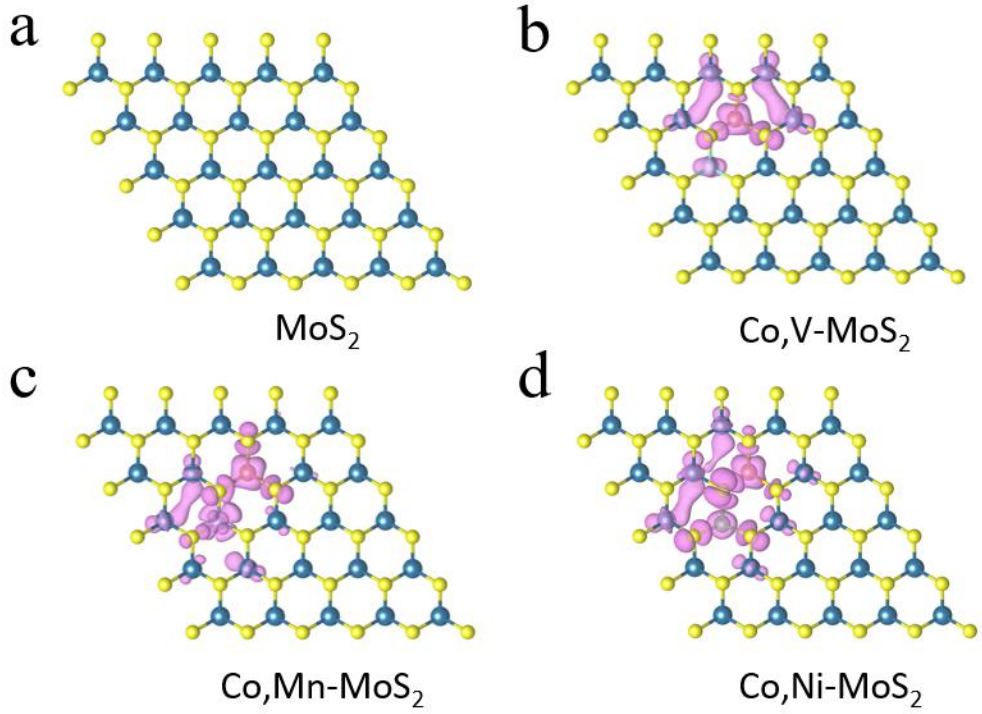

Supplementary Fig. 24 | Spin density plots of **a**, pristine MoS_2, **b**, Co,V-MoS_2, **c**, Co,Mn-MoS_2, and **d**, Co,Ni-MoS_2. Yellow, blue, red, cyan, purple, and green spheres denote S, Mo, Co, V, Mn, and Ni atoms, respectively. The light purple isosurfaces show the spin-state density.

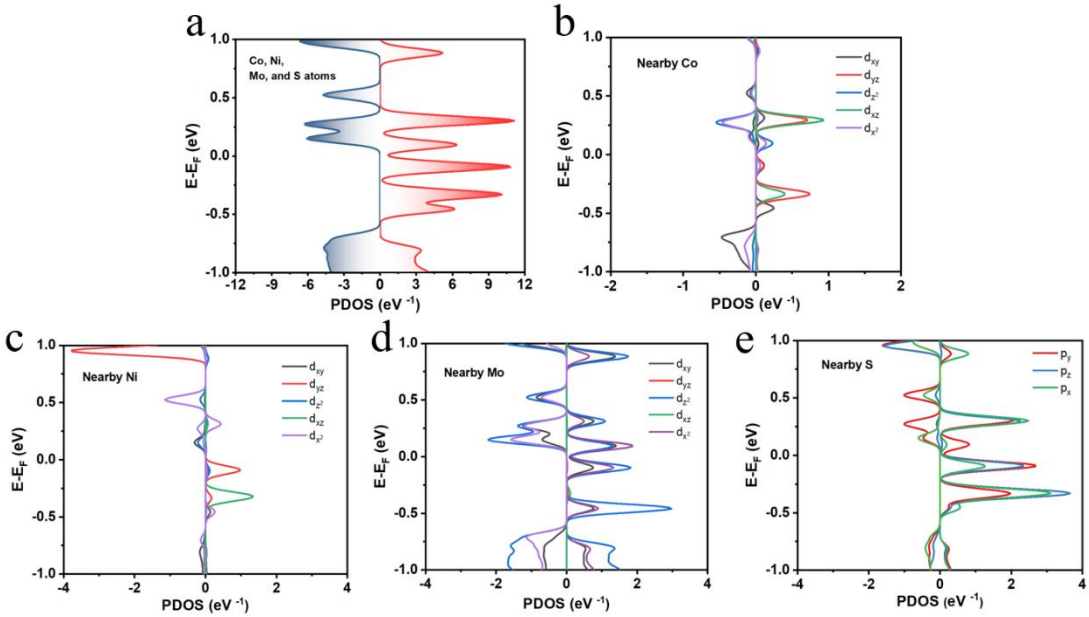

Supplementary Fig. 25 | a, The calculated DOS near the Fermi level for Co,Ni-MoS_2. **b**, Total density of states and projected density of states of individual, **c**, Co_{Mo} and **d**, Ni_{Mo} sites with **e**, nearby S, and **f**, Mo atoms in Co,Ni-MoS_2.

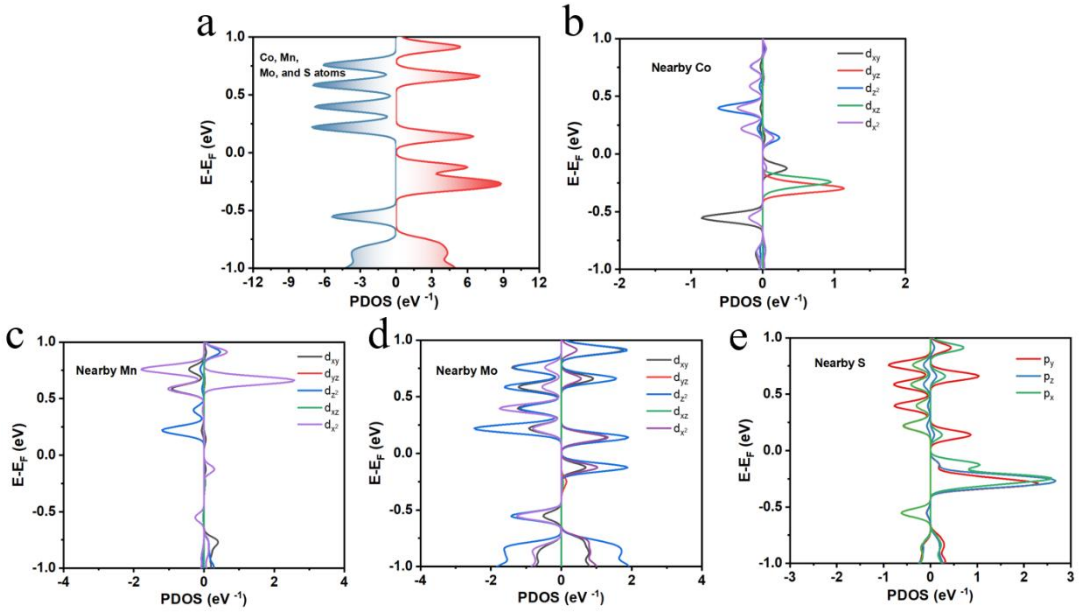

Supplementary Fig. 26 | **a**, The calculated DOS near the Fermi level for Co,Mn-MoS_2. **b**, Total density of states and projected density of states of individual, **c**, Co_{Mo} and **d**, Mn_{Mo} sites with **e**, nearby S, and **f**, Mo atoms in Co,Mn-MoS_2.

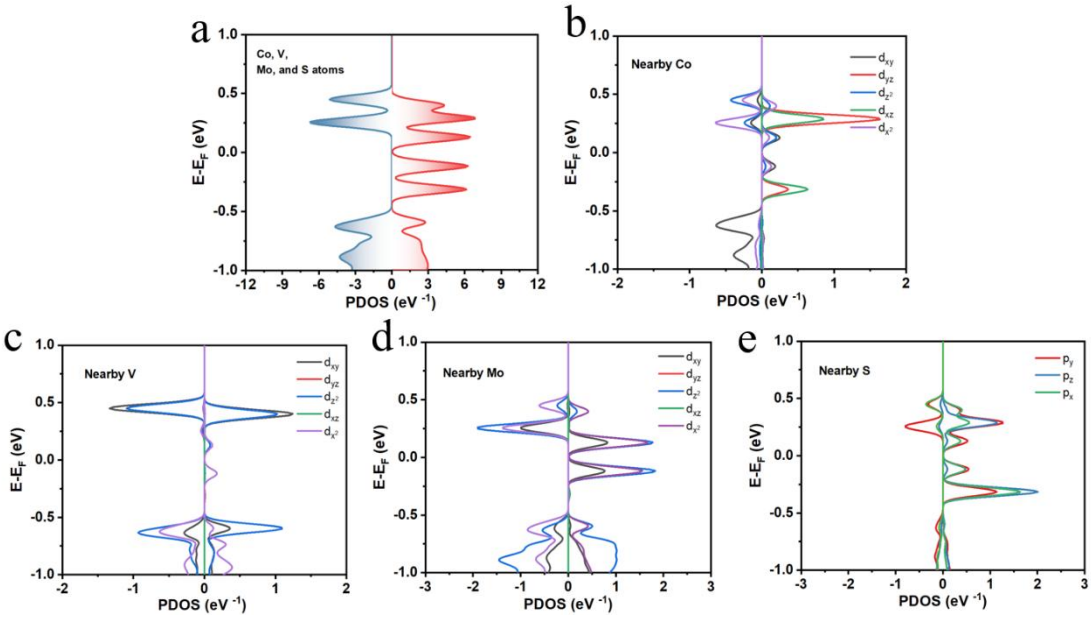

Supplementary Fig. 27 | a, The calculated DOS near the Fermi level for Co,V-MoS_2. **b**, Total density of states and projected density of states of individual, **c**, Co_{Mo} and **d**, V_{Mo} sites with **e**, nearby S, and **f**, Mo atoms in Co,V-MoS_2.

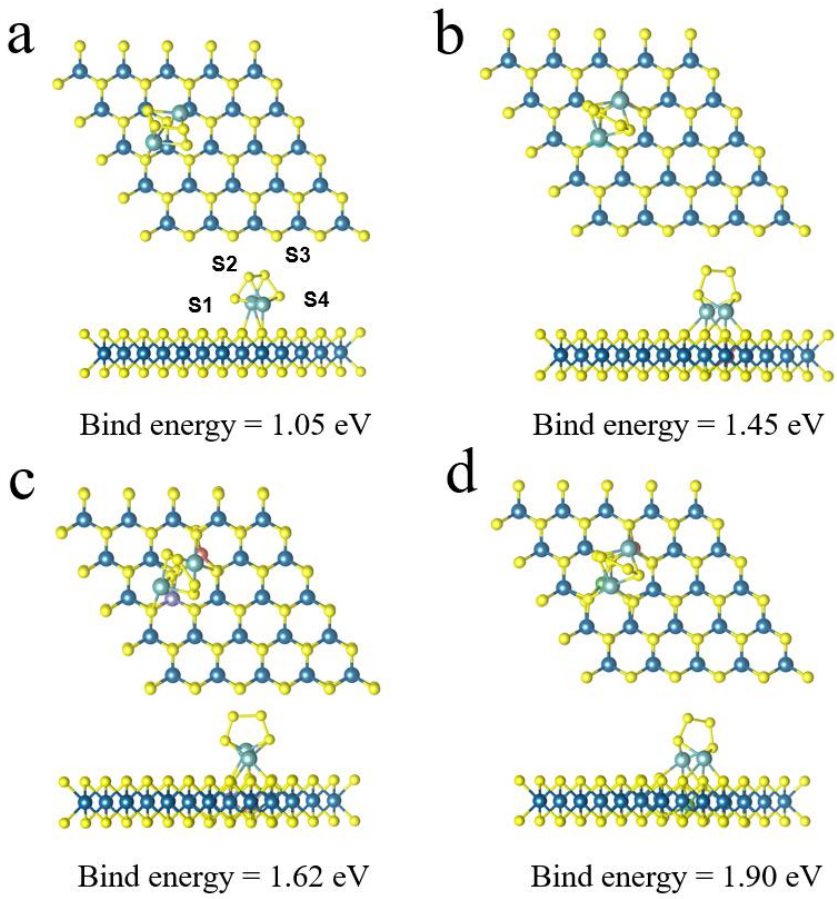

Supplementary Fig. 28 | Top view and side view of the optimized adsorption structures of Li_2S_4 on the **a**, MoS_2, **b**, Co,V-MoS_2, **c**, Co,Mn-MoS_2, and **d**, Co,Ni-MoS_2 surfaces, and the corresponding adsorption energies. Yellow, blue, slight blue, cyan, purple, green, and pink spheres denote S, Mo, Li, V, Mn, Ni, and Co atoms, respectively.

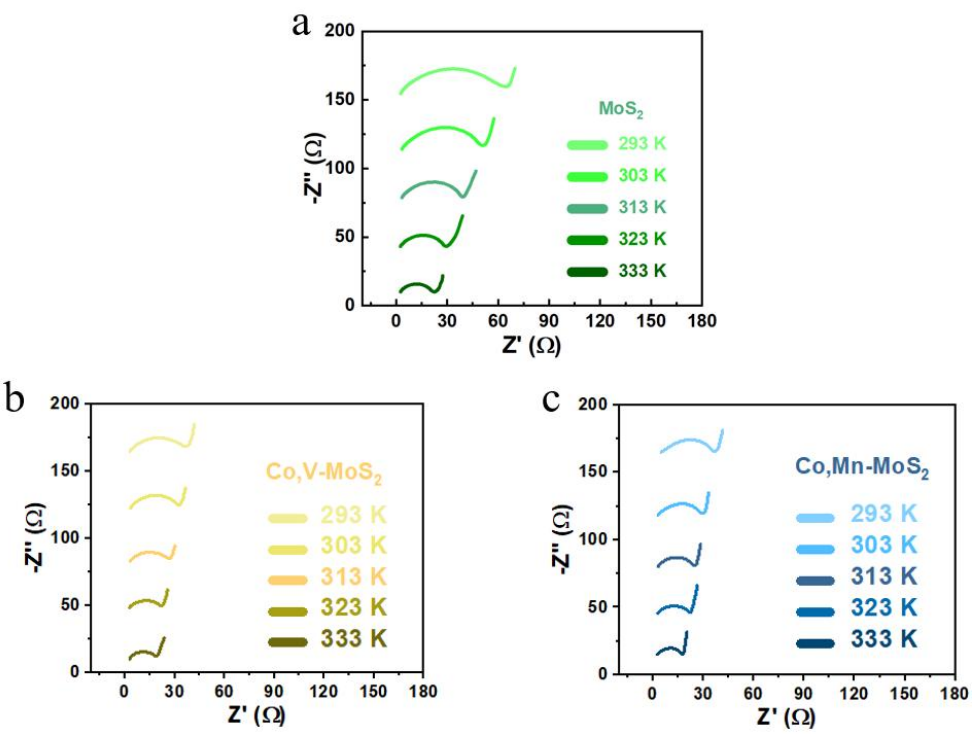

Supplementary Fig. 29 | EIS measurements for **a**, MoS_2, **b**, Co,V-MoS_2, and **c**, Co,Mn-MoS_2 catalysts at different temperatures.

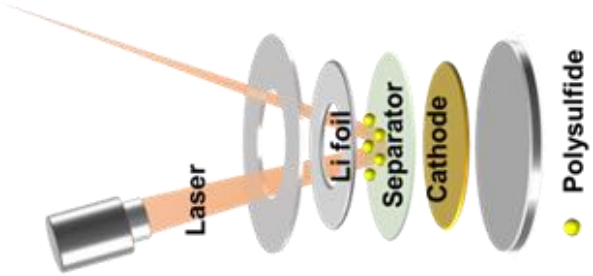

205

206

207 **Supplementary Fig. 30 |** Setup used for *in-situ* Raman spectroscopy analyses of the
208 cell configuration.

209

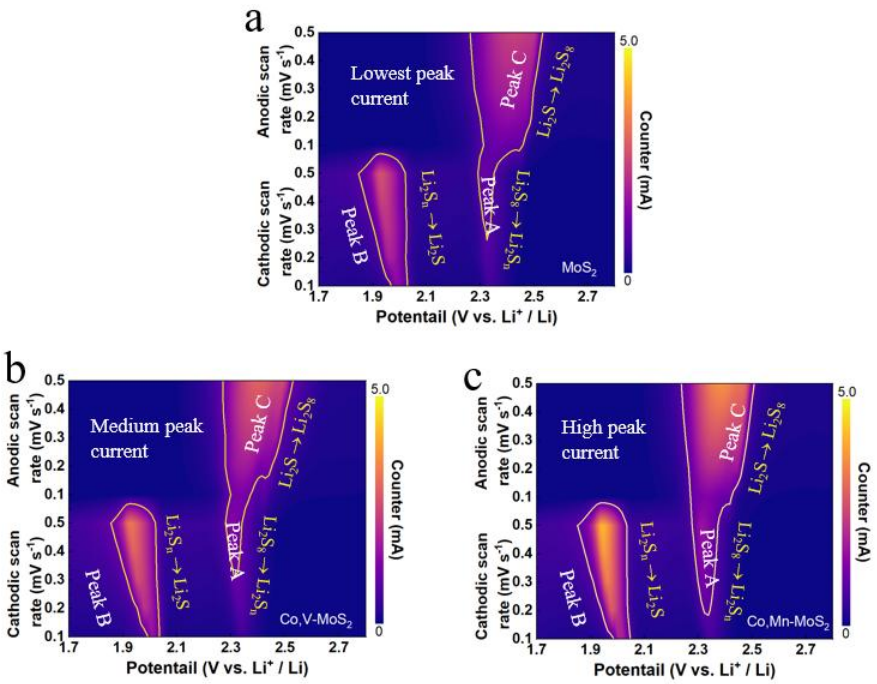

Supplementary Fig. 31 | CV profiles of **a**, MoS_2, **b**, Co,V-MoS_2, and **c**, Co,Mn-MoS_2-based cells were investigated at the different scan rates.

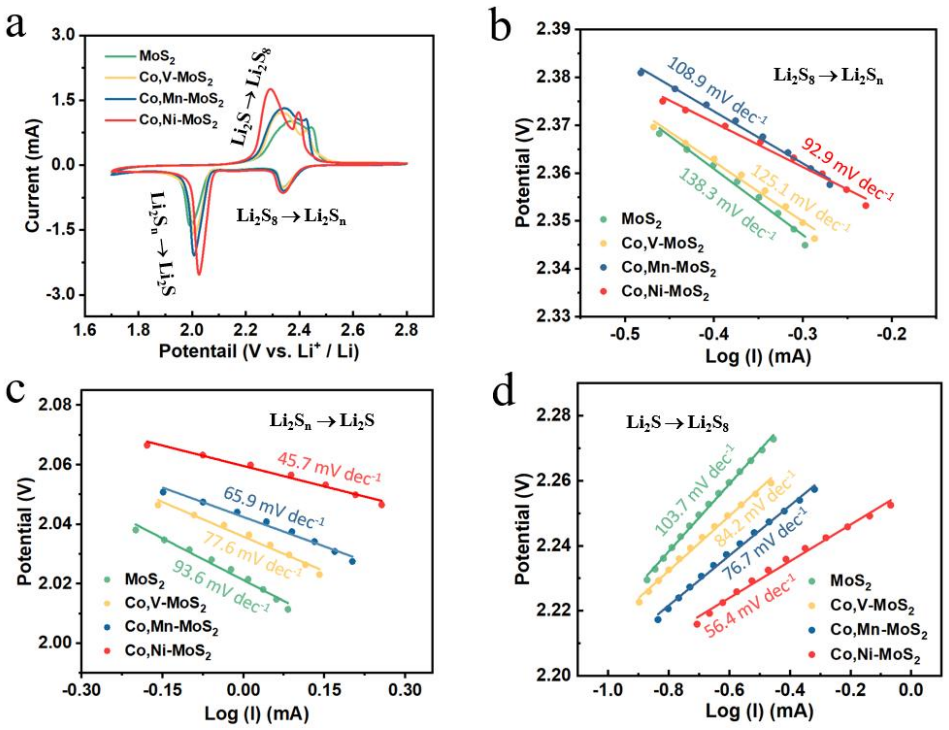

Supplementary Fig. 32 | a, CV profiles of the cells with different catalysts. The corresponding Tafel slopes of **b**, peak A, **c**, peak B, and **d**, peak C, from the CV profiles.

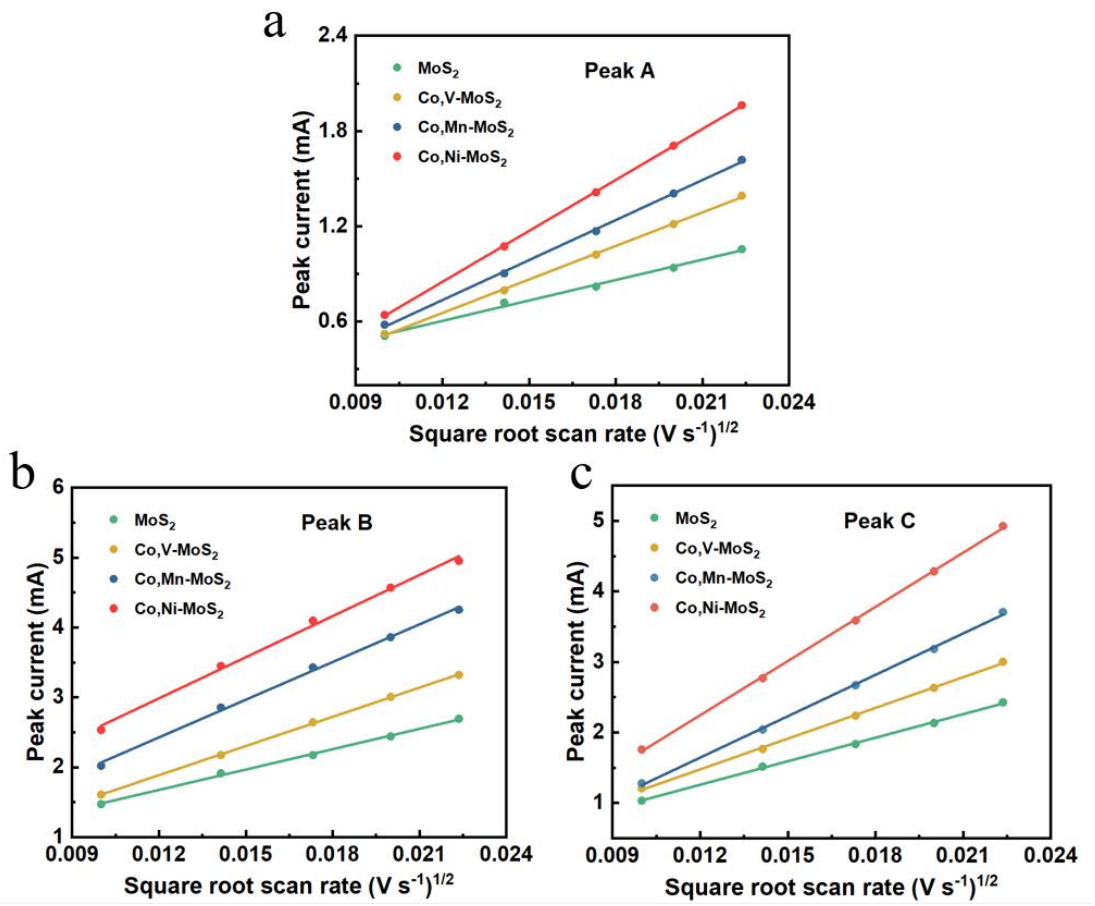

Supplementary Fig. 33 | a-c, Li-ion diffusion properties of MoS_2, Co,V-MoS_2, Co,Mn-MoS_2, and Co,Ni-MoS_2-based cell investigated by analyzing the CV peak currents for peaks (**a**) A, (**b**) B, and (**c**) C as a function of the square root of the scan rates.

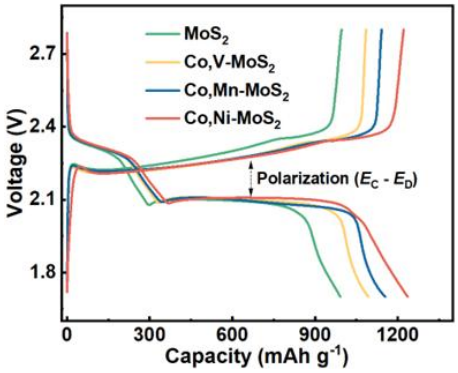

Supplementary Fig. 34 | Galvanostatic charge-discharge profiles with cells with the different catalysts and the corresponding polarization (E_C - E_D). E_C, charge voltage; E_D, discharge voltage.

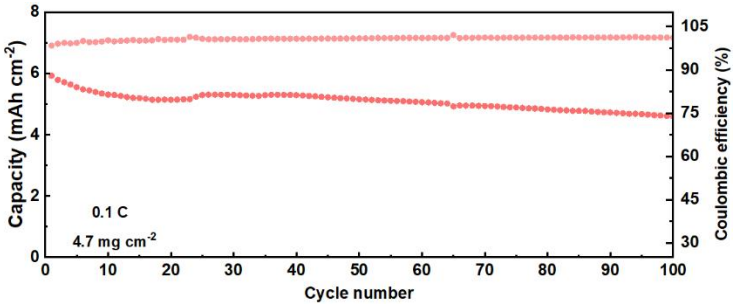

Supplementary Fig. 35 | Cycling performance of Co,Ni-MoS_2-based cells with a high sulfur loading of 4.7 mg cm^{-2} at 0.1 C.

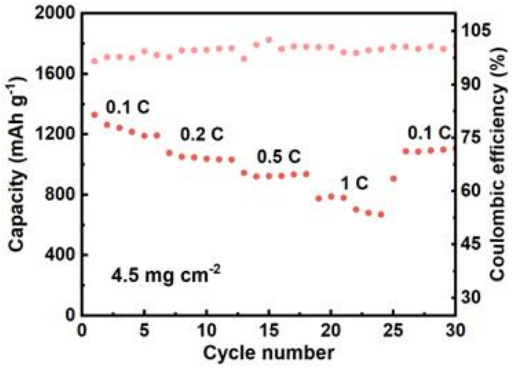

Supplementary Fig. 36 | Rate performance of a Co,Ni-MoS_2-based cell with a high sulfur loading of 4.5 mg cm^{-2} at 0.1 C to 1 C.

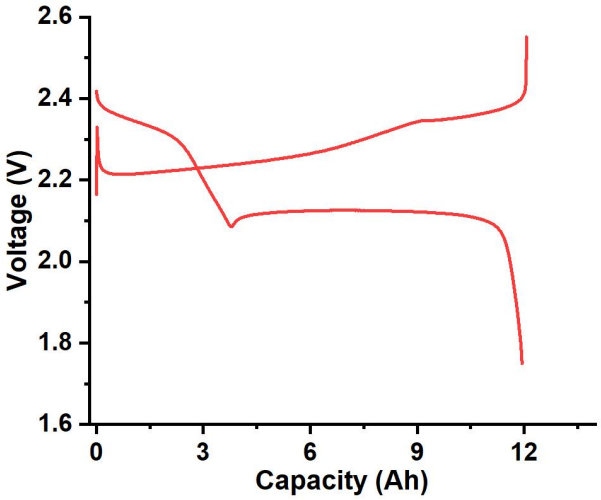

Supplementary Fig. 37 | Corresponding charge-discharge profiles of the 13.2 Ah-level pouch cells containing the Co,Ni-MoS_2 catalyst during the first cycle.

Supplementary Fig. 38 | Dimensions (length and width) of the pouch cell.

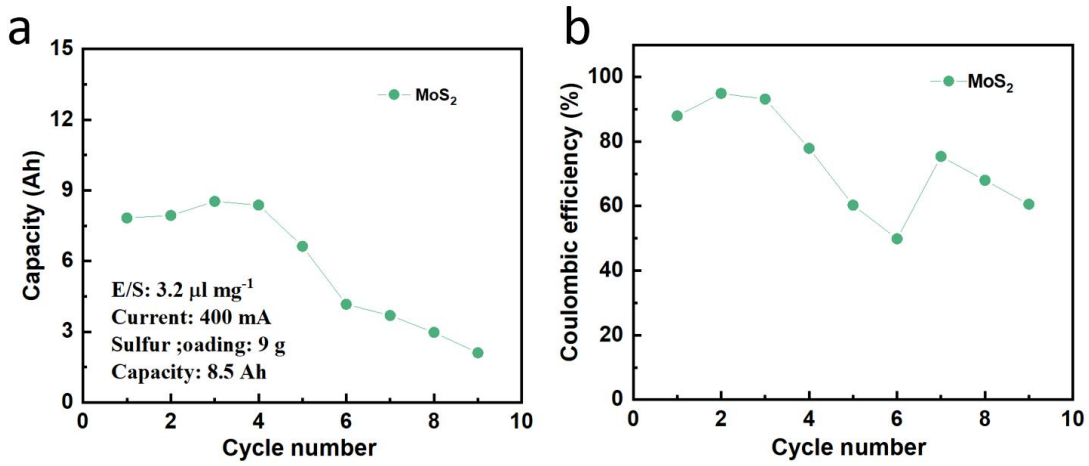

Supplementary Fig. 39 | a**,** Cycling performance and b, Coulombic efficiency of a MoS_2-based pouch cell with a high sulfur loading of 9 g at 400 mA.

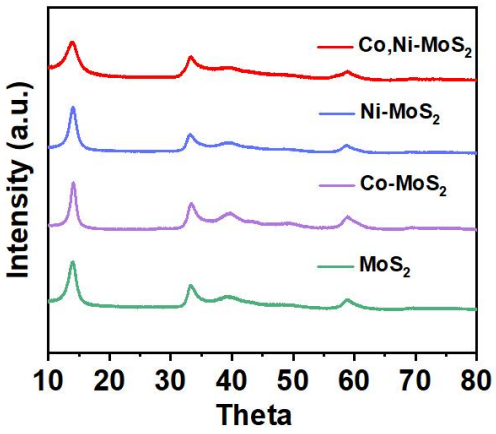

Supplementary Fig. 40 | XRD patterns of the catalysts doped with only Co or Ni.

In order to verify the advantage of Co,Ni-MoS_2 over MoS_2 doped with only Co or Ni, a series of experiments was performed. The materials were synthesized using the same methods as for Co,Ni-MoS_2, and XRD patterns were obtained. All the patterns agree with the data for MoS_2 (JCPDS card no. 37-1492).

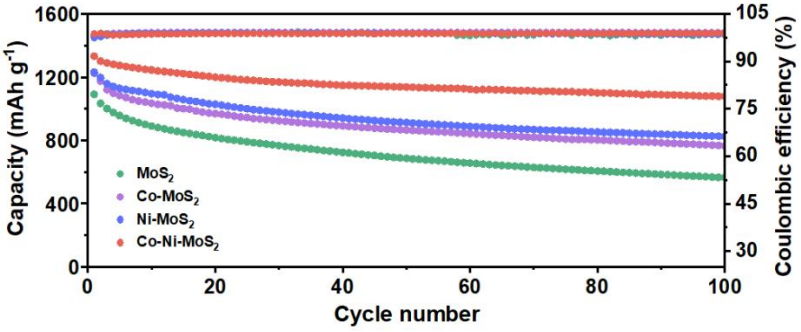

Supplementary Fig. 41 | Cycling performances of cells with the MoS_2, Co-MoS_2, Ni-MoS_2, and Co,Ni-MoS_2 catalysts at 0.3 C during the 100 cycles.

The electrochemical performance of the batteries using Co or Ni, or Co,Ni-MoS_2 catalysts has been thoroughly assessed. Subsequent cycling tests were conducted to evaluate the durability of the batteries. After 100 cycles at 0.3 C, the cells with Co or Ni doped MoS_2 retained a higher reversible discharge capacity than that with pure MoS_2. However, the Co,Ni-MoS_2-based cells had a much better performance, maintaining a capacity of 1077.5 mAh g^{-1} after 100 cycles. This clear contrast underscores the substantial performance improvements produced by the higher SRR catalytic activity.

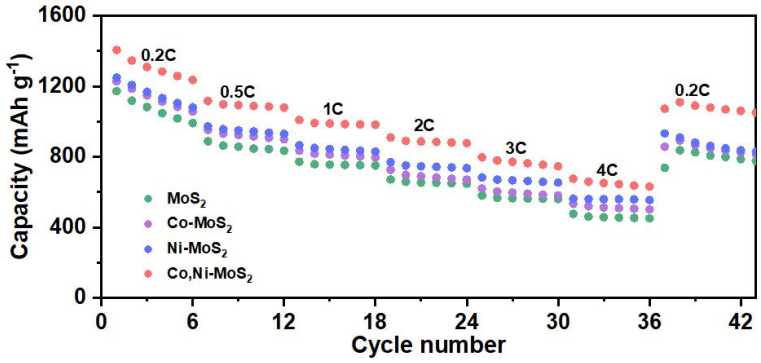

Supplementary Fig. 42 | Rate performance of MoS_2, Co-MoS_2, Ni-MoS_2, and Co,Ni-MoS_2 based-cells from 0.2 C to 4 C.

The rate performance of Li-S batteries using the different catalysts was tested at rates ranging from 0.2 C to 4 C and then back to 0.5 C. The Co,Ni-MoS_2-based cell had distinct charge and discharge plateaus, even at a high current rate of 4 C, and had outstanding reversible capacities of 1235, 982, and 631 mAh g^{-1} at 0.2 C, 1 C, and 4 C, respectively. In contrast, due to their lower catalytic efficiency, Co-MoS_2, Ni-MoS_2, and pure MoS_2-based cells had significantly lower capacities, particularly under high-rate conditions. These results are ascribed to differences in catalytic efficiency introduced by the incorporation of different metal cation pairs into MoS_2.

306 **Supplementary Table 1 |** The parameters considered in this study.
307

Number	Component features
1	Spin moment
2	Adsorption Li_2S
3	Adsorption Li_2S_2
4	Distance between metals
5	M1S min distance
6	M1S max distance
7	M1S avg distance
8	M2S min distance
9	M2S max distance
10	M2S avg distance
11	M1 covalent radius
12	M2 covalent radius
13	M1 atomic mass
14	M2 atomic mass
15	M1 melting point
16	M2 melting point
17	M1 ionization energy
18	M2 ionization energy
19	M1 valence electrons
20	M2 valence electrons
21	P band center
22	D band center
23	M1 D band center
24	M2 D band center
25	Mo D band center
26	M1 electronegativity
27	M2 electronegativity
28	Electronegativity of Mo in the active center
29	Electronegativity of S in the active center

308
309

Supplementary Table 2 | Metal contents in the MoS_2 host determined by ICP-MS analysis.

Samples	n_M:n_{Mo} (~at%)
Co,Ni-MoS_2	n_{Co}:n_{Mo} (4/100), n_{Ni}:n_{Mo} (4/100)
Co,Mn-MoS_2	n_{Co}:n_{Mo} (4/100), n_{Mn}:n_{Mo} (4/100)
Co,Ni-MoS_2	n_{Co}:n_{Mo} (4/100), n_V:n_{Mo} (4/100)

Supplementary Table 3 | Structural parameters and atomic positions of MoS_2 from Rietveld refinement.

Atom	Site	x	y	z
Mo	2c	0.33333	0.66667	0.25000
S	4f	0.33333	0.66667	0.62719

Supplementary Table 4 | Structural parameters and atomic positions of Co,V-MoS_2 from Rietveld refinement.

Atom	Site	x	y	z
Mo	2c	0.33333	0.66667	0.25000
S	4f	0.33333	0.66667	0.62162
Co	2c	0.33333	0.66667	0.25000
V	2c	0.33333	0.66667	0.25000

Supplementary Table 5 | Structural parameters and atomic positions of Co,Mn-MoS_2 from Rietveld refinement.

Atom	Site	x	y	z
Mo	2c	0.33333	0.66667	0.25000
S	4f	0.33333	0.66667	0.62388
Co	2c	0.33333	0.66667	0.25000
Mn	2c	0.33333	0.66667	0.25000

Supplementary Table 6 | Structural parameters and atomic positions of Co,Ni-MoS_2 from Rietveld refinement.

Atom	Site	x	y	z
Mo	2c	0.33333	0.66667	0.25000
S	4f	0.33333	0.66667	0.62393
Co	2c	0.33333	0.66667	0.25000
Ni	2c	0.33333	0.66667	0.25000

Supplementary Table 7 | Structural parameters extracted from the M K-edge EXAFS fitting.

Samples	Path	R (Å)	σ^2 (10^{-3} Å^2)	ΔE_0 (eV)	R-factor
Co,Ni-MoS_2	Co-S	2.22 ± 0.02	4.7	-9.73	0.006
Co,Ni-MoS_2	Ni-S	2.23 ± 0.01	8.2	-9.7	0.016
Co,Mn-MoS_2	Co-S	2.23 ± 0.05	4.9	-6.63	0.015
Co,Mn-MoS_2	Mn-S	2.26 ± 0.03	1.0	-6.24	0.014
Co,V-MoS_2	Co-S	2.22 ± 0.01	1.4	-9.9	0.009
Co,V-MoS_2	V-S	2.27 ± 0.07	5.6	-9.7	0.018

Supplementary Table 8 | The value of each parameter of the Ah level Li-S pouch cell.

Parameters	Value
Length (mm)	72
Width (mm)	113
Number of cathodes	18
Sulfur mass (g)	10.2
E/S ratio (μl mg^{-1})	3.2
Thickness of separator (μm)	9
Thickness of lithium anode (μm)	100
Total weight of battery (g)	67
Current density (mA)	1000
Capacity (Ah)	13.2
Energy density (Wh kg^{-1})	435

Supplementary Table 9 | Comparison of the electrochemical performances of various catalyst-based pouch cells between this work and other reported studies.

Areal S loading, mg cm^{-2}	E/S ratio, µl mg^{-1}	Total capacity, Ah	Specific energy density Wh kg^{-1}	Ref
9	**3.2**	**13.2**	**435**	**This work**
6.1	3.0	1.6	300	R[1]
NA	NA	1.17	313	R[2]
6	4	1.51	317	R[3]
12	5	2.5	330	R[4]
7.0	3.0	1.5	343	R[5]
6.0	2.3	6.2	351	R[6]
7.3	3.5 (g g_s^{-1})	2	353	R[7]
6.5	3.0	1.8	359	R[8]
10	1.2	NA	366	R[9]
17.3	4	1.82	402	R[10]
10	2.6	10	417	R[11]

Supplementary Note 1: Interpretable Multi-View Machine-Learned Framework

Data Collection

In this study, data collection was carried out based on first-principles calculations. The two atom doping configurations of MoS_2 are illustrated in Supplementary Fig. 1. Using density functional theory (DFT), we calculated the energy barriers of the rate-determining step (ΔG) for the Li_2S_2-to-Li_2S conversion on various dual-doped MoS_2 surfaces.

Parameter Selection

To ensure effective model construction and enable interpretable insights into underlying chemical principles, we established three core criteria for feature selection: (1) features must be closely related to the catalytic performance of the material to ensure clear physical meaning; (2) features should accurately represent the geometric structure of the material; and (3) features should be easily obtainable and reproducible, facilitating data extension and model transferability.

Building upon previous research, we further expanded the feature space. Previous studies have demonstrated a strong correlation between adsorption energy and catalytic activity; thus, the adsorption energies of Li_2S_2 and Li_2S on catalyst surfaces were included as key features. According to the Sabatier principle, the electronic structure of active catalytic sites plays a pivotal role in determining catalytic behavior. Therefore, we incorporated several electronic descriptors, including spin density, the d-band center of transition metals, the p-band center of non-transition metals, and the charge transfer induced by doping.

In addition, various fundamental physicochemical properties potentially affecting

catalytic performance were considered, such as the first ionization energy of the metal atoms and the Pauling electronegativity of active-site elements (including both metals and non-metals). To more comprehensively capture the structural characteristics of the materials, geometric and electronic structure parameters such as bond lengths, charge distributions, and d-band centers corresponding to different doping elements were also included.

We also augmented the feature set with elemental properties sourced from the Mendeleev database, incorporating descriptors such as atomic mass, valence electron count, and melting point. These physicochemical features were used to construct machine learning models targeting the reaction free energy change (ΔG), with the aim of uncovering the key factors influencing catalytic performance. Details and definitions of the elemental property data can be found at: https://mendeleev.readthedocs.io/en/stable/data.html.

Selection of Machine Learning Methods

In this study, multiple machine learning algorithms were employed to analyze and predict target features, including Random Forest Regressor, Least Absolute Shrinkage and Selection Operator (LASSO) regression, Ridge Regression, and eXtreme Gradient Boosting (XGBoost) Regressor. By comparing the predictive performance of these models, the objective was to identify the most suitable algorithm for the specific tasks of this research.

To increase the robustness of model evaluation, the Leave-One-Out Cross-Validation approach was adopted. In each iteration of this method, a single data

point was held out as the validation set while the remaining samples were used for training. This process was repeated until every sample has served once as the validation set. This validation strategy effectively reduces model bias and improves generalization performance.

Hyperparameter Optimization of Regression Models

To improve the regression models, a hybrid strategy combining automated search and manual tuning was employed for hyperparameter optimization. Initially, potential optimal hyperparameter combinations were identified using automated techniques such as Grid Search. Subsequently, fine-tuning was performed manually based on model performance on the validation set, aiming to improve both generalization ability and predictive accuracy.

Specifically, for the Random Forest Regressor, key parameters such as the number of data and the maximum data depth were optimized. For the LASSO Regressor, a systematic exploration of different regularization strengths (α) was conducted to determine the most appropriate level of sparsity. Similarly, for the Ridge Regressor, the regularization parameter (α) was optimized through a combination of automated and manual tuning to achieve a balanced performance across both training and validation datasets. For the XGBoost Regressor, a joint optimization of critical parameters such as the number of estimators, maximum depth, and learning rate was carried out to maximize predictive accuracy.

During each round of cross-validation, model performance was quantitatively assessed by recording the Mean Squared Error (MSE) and the Coefficient of

Determination (R^2). These metrics were used to compare and evaluate the effectiveness of each regression model.

$$R^2 = 1 - \frac{\sum_i (Y_i - y_i)^2}{\sum_i (Y_i - \bar{Y})^2}$$

$$\mathrm{MSE} = \frac{1}{N}\sum_{i}^{n} (Y_i - y_i)^2$$

Y_i represents the true values obtained from DFT calculations, while y_i denotes the predictions made by the machine learning models, and Y is the mean value of the DFT data. An ideal model should have an R^2 value close to 1 and an MSE value close to 0. Ultimately, the hyperparameter combination that performs best on the validation set is selected as the final configuration for each model. The performance of the different models across various metrics is shown in Supplementary Fig. 13.

Feature Importance Analysis

The SHapley Additive exPlanations (SHAP) method, proposed by Lundberg and Lee in 2017, is based on the Shapley values from cooperative game theory and is designed to provide interpretable explanations for model predictions. In this study, we used SHAP to perform a posteriori quantitative assessment of feature importance, aiming to estimate the contribution of each input feature to the model's predictive outcomes. For each individual data point, SHAP perturbs the input features and computes their marginal contributions to the prediction, resulting in a corresponding "importance value." By aggregating SHAP values across all samples and calculating the mean, we can further evaluate the global importance of each feature within the entire dataset.

This dual capability enables SHAP to offer both local interpretability (explaining individual predictions) and global interpretability (assessing feature impact across the entire model), making it a powerful and widely applicable tool. Features with higher importance exhibit larger SHAP values, while less influential features tend to have smaller or near-zero SHAP values.

As a model-agnostic interpretation framework, SHAP can be applied to various machine learning models, allowing for a transparent visualization and understanding of how input features influence the model's decision-making process. In this work, we used SHAP to analyze six key features in our model, thereby identifying the variables with the most significant impact on prediction outcomes.

The SHAP value for a feature was computed using the following formula:

$$\Phi_i = \sum_{S \subseteq F, \{i\}} \frac{|S|!(|F| - |S| - 1)!}{|F|!} \left[f_{S \cup \{i\}}(x_{S \cup \{i\}}) - f_S(x_S) \right]$$

Φi denotes the SHAP value of feature i, S is a subset of the full feature set F, X_S represents the input values corresponding to subset S, and f_S is the output function of the trained model. By evaluating the change in model output when feature i is added to subset S, the marginal contribution of feature i can be quantitatively determined.

Supplementary References

1. X. Q, Zhang. et al. Electrolyte Structure of Lithium Polysulfides with Anti-Reductive Solvent Shells for Practical Lithium-Sulfur Batteries. Angew. Chem., Int. Ed. 2021, 60, 15503-15509 (2021).

2. Niu, C. J. et al. High-energy lithium metal pouch cells with limited anode swelling and long stable cycles. Nat. Energy 4, 551-559 (2019).

3. Zhao, C. et al. A high-energy and long-cycling lithium-sulfur pouch cell via a macroporous catalytic cathode with double-end binding sites. Nat. Nanotechnol. 16, 166-+ (2021).

4. Huang, Y. Y. et al. Sulfur Cathodes with Self-Organized Cellulose Nanofibers in Stable Ah-Level, >300 Wh kg-1 Lithium-Sulfur Cells. Adv. Energy Mater. 12, 2202474 (2022).

5. Zhao, C. X. et al. Semi-Immobilized Molecular Electrocatalysts for High-Performance Lithium-Sulfur Batteries. J. Am. Chem. Soc. 143, 19865-19872 (2021).

6. Shi, L. L. et al. Reaction heterogeneity in practical high-energy lithium-sulfur pouch cells. Energy Environ. Sci. 13, 3620-3632 (2020).

7. Song, Y. W. et al. Cationic lithium polysulfides in lithium-sulfur batteries. Chem 8, 3031-3050 (2022).

8. Yao, W. Q. et al. Dynamic Intercalation-Conversion Site Supported Ultrathin 2D Mesoporous SnO2/SnSe2 Hybrid as Bifunctional Polysulfide Immobilizer and Lithium Regulator for Lithium-Sulfur Chemistry. ACS Nano 16, 10783-10797 (2022).

9. Xue, W. J. et al. Intercalation-conversion hybrid cathodes enabling Li-S full-cell architectures with jointly superior gravimetric and volumetric energy densities. Nat. Energy 4, 374-382 (2019).

10. Han, Z. Y. et al. Machine-learning-assisted design of a binary descriptor to decipher electronic and structural effects on sulfur reduction kinetics. Nat. Catal. 6, 1073-1086 (2023).

11. Huang, Z. M. et al. Multifunctional Ultrathin Ti3C2Tx MXene@CuCo2O4 /PE Separator for Ultra-High-Energy-Density and Large-Capacity Lithium-Sulfur Pouch Cells. Adv. Mater. 37, 2410318 (2024).